Version of Record: https://www.sciencedirect.com/science/article/pii/S0921509321005876
Manuscript_3e29f0ed4ee79eabdb2d2fe9a7807ed7

Microstructural and mechanical characterization of a shot peening induced rolled edge on direct aged Inconel 718 alloy

S. Breumier[1,*], F.Adamski,[2] J.Badreddine,[2] M. Lévesque,[3] G. Kermouche[1]

[1]Mines Saint-Etienne, Univ Lyon, CNRS, UMR 5307 LGF, Centre SMS, F - 42023 Saint-Etienne, France

[2]Safran Tech, rue des Jeunes Bois Châteaufort CS 80112, Magny les Hameaux, 78772 France

[3]Département de Génie Mécanique, École Polytechnique de Montréal, C.P. 6079, Succ. Centre-ville, Montréal, Québec, H3C 3A7 Canada

Abstract

Shot peening of complex geometries can generate rolled edges which mechanical properties, compared to a flat shot peened specimen, are not well known. Electron BackScattered Diffraction (EBSD) analyses and nanoindentation tests were conducted to characterize the microstructural changes and hardening induced in the rolled edge compared to a reference flat part of an Inconel 718 direct aged specimen. Dictionary Indexing was used to improve the indexation quality in zones presenting severe plastic deformations. Geometrically necessary dislocation densities were estimated from the EBSD orientation maps and correlated with the nanoindentation measurements using a Taylor hardening model. The rolled edge zone presented 1 GPa higher hardening values and a steeper hardening gradient as compared with the reference. This was mainly attributed to work hardening, due to higher dislocation densities around the rolled edge. Such differences could result from a pure shear state induced by bending of the surface close to the sample's border during the rolled-edge formation.

*Corresponding author.
Email: simon.breumier@mines-saint-etienne.org
Tel: +33 (0)4 77 42 02 95

Keywords: Rolled edge, shot peening, Dictionary indexing, Geometry necessary dislocations, EBSD

Introduction

Shot peening is a surface mechanical treatment widely used in the industry to enhance the properties of treated parts in terms of fatigue resistance [24, 10, 16], hardness [25, 40, 47] or stress-corrosion cracking resistance [3, 31]. However, quantitatively predict the process benefits in terms of fatigue life remains a challenge. The process has been extensively studied and it is now possible to model a large number of shot from the nozzle to the treated part's material [11, 13, 18, 39, 20].

Several works focused on the application of such models on complex geometries for industrial applications [9, 6, 11, 12]. Most of these approaches assumed that shot peening involved similar strain mechanisms in a flat sample than in a complex geometry. For instance, Gallitelli et al. [11] modeled the shot peening of a spur gear by computing the residual stress field induced by single impacts of different velocities. These fields were then introduced in the geometry using the eigenstrains method, following an impact velocity field predicted by a discrete element model.

Shot peening of geometric singularities, such as sharp corners or holes, can induce a bulge at the border of the treated part. This situation results from the peened material's stretching and rolling over the sharp corner onto the orthogonal face. As the material rolls onto itself, these bulges are often referred to as rolled edges or "elephant-tails". The influence of such rolled edge on fatigue life has been investigated by a few authors both in Low cycle Fatigue (LCF) and High Cycle Fatigue (HCF) regimes [17, 45, 22, 38]. Klotz et al. [22] and Sun et al. [38] investigated the influence of the initial edge geometry on the fatigue life of shot peened parts respectively for the Inconel 718 alloy and the Ti-17 alloy. Differences in crack initiations were related by both studies to rolled-edges acting as local stress concentrators resulting in a shorter fatigue life. In particular, Sun et al. [38] revealed that significant rolled edges could result in a shorter fatigue life than that of an unpeened specimen. He et al. [17] and You et al. [45] also showed that removing the rolled-edge by grinding would improve the

sample's LCF life. Understanding rolled-edges formation and material properties is therefore crucial as it could cancel all the beneficial effects of the process.

Apart from such geometrical effect, the material's mechanical properties induced in the rolled edge were scarcely investigated. Sun et al. [38] performed finite element simulations of Laser shot Peening (LSP) on a specimen edge. The authors found that rolled edges presented larger plastic strains and higher compressive stress values as the laser shock waves interacted with the sample edges. Such result was however not confirmed experimentally, nor reported for conventional shot peening, for which shock wave intensities are negligible when compared to those occurring during LSP. A modified microstructure and hardening state could play a crucial role in the material's local hardness, mechanical properties or corrosion resistance, thus possibly impacting the material's fatigue life.

Advances in the past thirty years in Electron BackScattered Diffraction (EBSD) characterization methods could provide insights on such heterogeneous hardening. Based on indexation of Kikuchi bands on the electron diffraction pattern, the technique can measure a material orientation distribution, hence providing access to the local microstructure, Geometrically Necessary Dislocation (GND) distribution lower bound and residual stress distribution. Wright et al. [43] introduced alternative indexing methods such as Dictionary Indexing (DI) to perform EBSD observations on surfaces producing noisy diffraction patterns. The method was successfully applied on shot peened materials by Singh et al. [37] and on materials presenting pattern similarities by Burch et al. [5] or pseudo-symmetries by Degraef et al. [8]. Such method could therefore provide a rich characterization tool for highly deformed structures, such as rolled edges.

In particular, as demonstrated by Pantleon [32], misorientation maps generated by EBSD can provide an estimate of the GND density distribution. Such estimation relies on a relation between the Nye tensor and the local lattice curvature. However, this method only provides a lower bound of the GND density as it relies on the hypothesis that the observed surface is in a plane stress state, as pointed out by Wilkinson et al. [42]. Also, the method usually neglects the elastic strain contribution to the lattice curvature, which could lead to substantial errors, as demonstrated by Acharya et al. [2]. It could however provide insights in the work hardening gradients resulting from surface process treatments.

Other hardening sources could contribute to the material's mechanical properties, such as the Hall-Petch effect, residual stresses or precipitate hardening. Wu et al. [44] used nanoindentation and Atomic Force Macroscopy (AFM) measurements to investigate the interplay of residual stresses and grain refinement induced by Surface Mechanical Attrition Treatment (SMAT) on the hardness gradient of a 316L steel. Tumbajoy-Spinel et al. [41] combined nanoindentation testing, micropillar compression and Kernel Average Misorientation (KAM) maps to decorrelate the effect of each hardening contributions on micro-percuted surfaces. As pointed out by the authors, instrumented nanoindentation testing provides a local estimate of the material's hardening gradients considering all the contributions. Such test could therefore be combined with EBSD GND estimations to decorrelate work hardening from other sources.

The objective of the present work is to characterize the differences in microstructure and hardening induced in a rolled edge compared to a reference flat shot peened surface. First, microstructural evolutions in the rolled edge were characterized using EBSD with Dictionary Indexing (DI). GND densities were estimated using the method described by Pantleon [32]. The ability of DI, when compared with the usual Hough indexing, to extract misorientation in the shot peened zone was investigated. DI was then used to compare the rolled edge hardening state with a shot peened reference taken at the sample center. Finally, GND density variations were related to instrumented nanoindentation measurements to assess the differences in mechanical properties in the rolled edge zone due to work hardening.

The novelty of our work resides in combining EBSD GND analyses and nanoindentation hardness measurements to investigate the signature of the shot peening process in the vicinity of a sample's corner to provide concrete recommendations regarding the removal of a rolled-edge induced by shot-peening in an industrial context.

1 Materials and methods

1.1 Sample preparation

Inconel 718 Direct Aged parallelepipedic samples with sharp edges and a section measuring 0.5 mm×15 mm were shot peened with a 0.22 mmA intensity and a 400% coverage using the set-up schematized in Figure 1. The shot peening treatment induced rolled edges

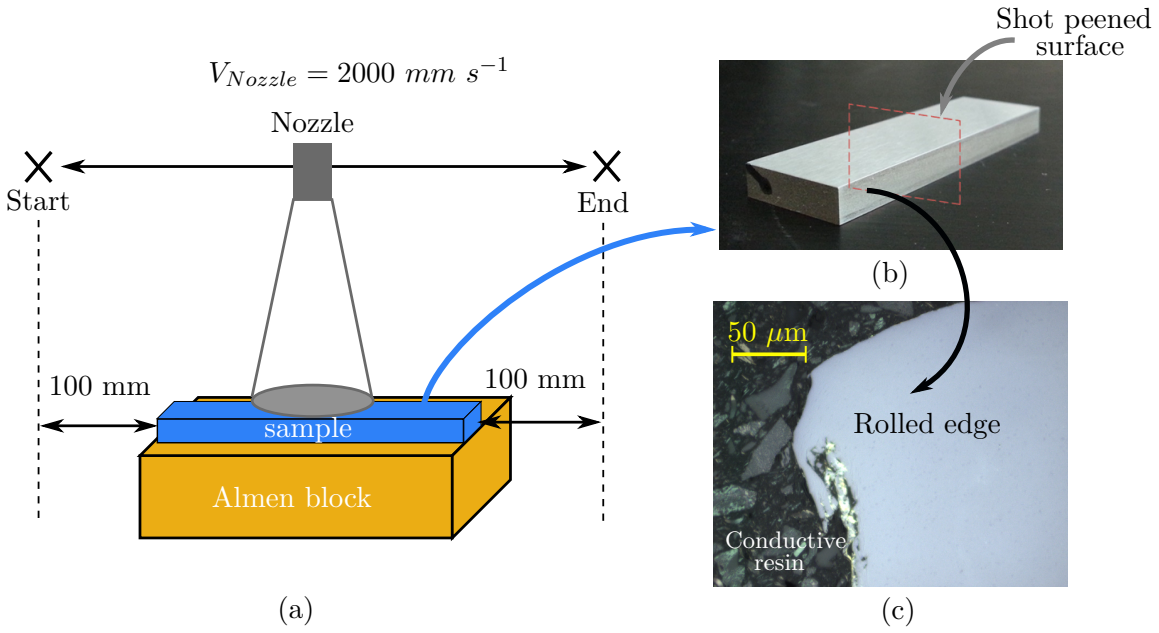

Figure 1: (a) Schematic of the shot peening set-up used in this study. (b) shot peened sample. (c) Micrograph showing the shot peening induced rolled edge. The nozzle velocity V_{Nozzle} was 2000 mm s^{-1}. Shot peening at the sample's borders induced rolled edge as visible on the micrograph at the bottom right.

at the sample's border, as shown in the micrograph represented in Figure 1. A 10 mm long sample was then cut using a Niobium carbide circular saw and coated in a conductive resin (PolyFast, Struers) for automatic polishing. The sample was then mechanically polished with P200 to P1000 SiC grit paper then successively with a 3 μm and 1 μm diamond suspension (Metadi, Buehler) and vibro-polished during one night using a Mastermet solution (Buehler). A 1.25 nm Platinium layer was finally deposited on the sample to make the observation surface fully conductive, using a Leica ACE600 high vacuum sputter coater. The coating limited electron beam drifting when observing the sample's extreme surface during EBSD acquisition.

1.2 EBSD analysis

Pattern acquisition

The EBSD acquisition was performed using a Zeiss Merlin equipped with a Field Emission Gun (FEG) Gemini 2 column. EBSD patterns were captured using a Brucker e-FlashFS camera with a 70° tilt angle at 20 kV acceleration voltage, 20 nA probe current and a 150 nm step. The pattern resolution was 160×120 (4×4 binning) and six patterns were averaged for

Crystal system	Lattice Parameter	Space Group	Atomic Number	Debye-Waller factor
1 (cubic)	0.35236 nm	225	28	0.0035 nm^2

Table 1: Parameters used to generate the Dictionary Indexing master file [19]

each measured point to reduce noise. Only the austenitic face-centered cubic matrix γ was indexed.

Two EBSD maps were successively captured at the rolled edge and from the rolled edge to the sample's flat part to observe the full property gradient induced close to the sample's border. A third map was also performed in the sample's bulk to compare the surface properties with the reference non-peened material.

Dictionary indexing

Indexation of the Kikuchi pattern is classically performed by detecting the pattern's bands using the Hough transform. However, this technique usually fails to characterize severe plastic deformations as it usually results in noisy patterns, making band detection difficult. Dictionary indexing (DI) is based on the comparison of a diffracted pattern with dynamically simulated patterns generated from an orientation subspace. Since it does not rely on band detection, it is therefore more robust toward noise induced by plastic deformations.

Diffraction patterns were indexed using the Dictionary Indexing (DI) method implemented in the *EMsoft* software following the methodology developed by Jackson et al. [19]. A master pattern was generated using the *EMsoft* forward model with the input parameters given in Table 1. This master pattern was then used to discretize the orientation space using 100 cubochoric samples for a first raw indexation. The indexing success threshold angle was set to 1.5°. The indexed points' orientations were then refined by orientation space subsampling close to the first solution using the *EMFit* program, with a 0.03 refinement step size.

GND estimations

GND density distributions were estimated using the *Matlab mtex* toolbox introduced by Bachmann et al. [4] following the methodology described by Pantlon [32]. The methodology is based on the determination of the Nye tensor $\boldsymbol{\alpha}$ with the EBSD misorientation data ω at

each point with:

$$B^s = \int_S \boldsymbol{\alpha} \cdot \mathbf{n} dS = -\int_S \mathrm{curl}((F^e)^{-1}) \cdot \mathbf{n} \mathrm{d}S, \tag{1}$$

$$B^s = \int_S \boldsymbol{\alpha} \cdot \mathbf{n} dS = \left(\int_S \mathbf{t^s} \cdot \mathbf{n} dS \right) \cdot \mathbf{b^s}, \tag{2}$$

where B^s is the resulting Burgers vector in the gliding system s when integrating on a surface element S of normal $\mathbf{n}$, F^e is the elastic part of the deformation gradient tensor and $\mathbf{t^s}$ and $\mathbf{b^s}$ are respectively the dislocation line and Burgers vector in the gliding system s. By neglecting the elastic distortions contribution to the curl of the elastic deformation tensor, the above relations yield:

$$\boldsymbol{\alpha} = \sum_s \rho^s \mathbf{b^s} \otimes \mathbf{t^s} \approx \mathrm{curl}(\omega), \tag{3}$$

where ρ^s is the GND density in the gliding system s.

For face-centered cubic structures, 18 slip systems are usually chosen (12 pure edge and 6 pure screw dislocations). Four out of the nine components of $\boldsymbol{\alpha}$ are unknown, as EBSD only provides in-plane measurements. Identifying ρ^s for every system s from Equation 3 is therefore an ill-posed problem and requires to minimize another physical quantity to be solved. Let us introduce the total dislocation line energy defined as:

$$\Psi = \sum_s \rho^s u^s, \tag{4}$$

where u^s is the system s dislocation line energy defined as:

$$u^s = \begin{cases} \frac{b^2}{1-\nu} & \text{for edge dislocations} \\ b^2 & \text{for screw dislocations} \end{cases},$$

where ν is the material's Poisson's ratio taken as 0.3 and b is the norm of the Burgers vector taken as 0.26 nm. The quantity ρ^s for each system s is found by minimizing Ψ under the constraint defined by equation 3.

It should be noted that the methodology therefore only provides a lower bound of the GND density [42]. It can however be used for comparison purposes. Also, the chosen minimized quantity should only have little effect on the total dislocation density [7], which was the only

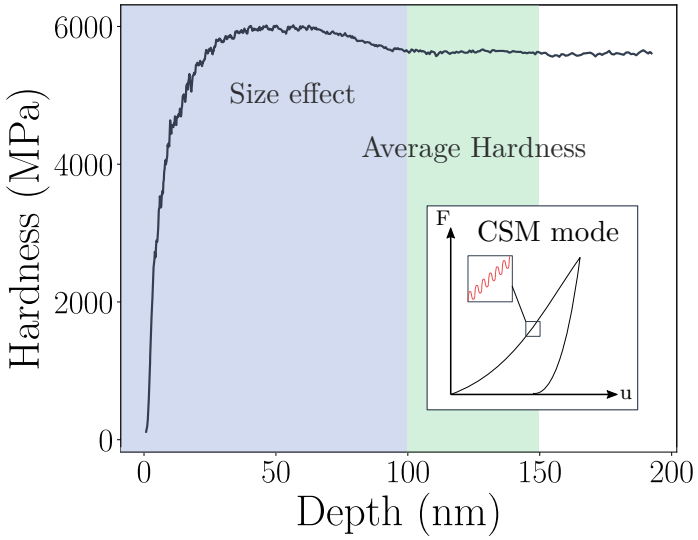

Figure 2: Typical hardness variation with indentation depth obtained using the CSM mode. An oscillating displacement is imposed to the indenter during the test, hence providing a continuous measure of the material's hardness and reduced modulus with indentation depth. Size effects down to 100 nm results in higher hardness values. The final hardness value is taken as the average in the stable zone, between 100 nm and 150 nm.

quantity considered in this work.

1.3 Nanoindentation

Nanoindentation tests were performed to map the process induced hardness gradient close and far from the rolled edge. A MTS DCM nanoindenter with a diamond Berkovitch tip was used. The test consists in indenting a material's surface using a diamond tip down to a few hundred micrometers while measuring the indentation load and displacement. The material hardness is then obtained by estimating the contact surface between the tip and the indented material.

The nanoindenter Continuous Stiffness Measurement (CSM) mode developed by Oliver et al. [30] was used. An oscillating displacement was imposed to the tip at a 75 KHz frequency allowing the continuous measurement of the contact stiffness. In the present work, it was considered that the elastic modulus remained the same wherever the indentation was performed. This provided hardness estimations without any assumption on the contact geometry, nor on the material's residual stress state.

At small indentation depth, size effects resulting from the small dimensions of the loaded

volume could occur. Such size effects usually result in higher hardness values at small depths, as the loaded volume to dislocation density ratio is not representative of the bulk. As illustrated in Figure 2, the method provides insights in the depth where size effects occur, as the measured hardness is higher at lower depths. The final hardness measurement is then given as the hardness average in the zone where the hardness becomes constant. In this study, the hardness value was obtained by averaging hardness values for depths varying from 100 nm to 150 nm depth. This also ensures that the estimated hardness were estimated in the autosimilarity regime as the estimated defect height of the tip used in this study is around 7 nm [15]. Indentations were performed with a load control set-up. The indentation depth was limited to 200 nm.

2 Results

2.1 Microstructure analysis

Figure 3 shows an assembly of the two Inverse Pole Figures (IPF) relative to the sample's normal obtained using the dictionary indexing method from the rolled edge to the sample's flat part. A drift in the orientation data between the two maps can be observed and results from EBSD beam drift due to the long time required for the acquisition.

Large plastic deformation close to the rolled edge led to lower indexing rates, even using the dictionary indexing method. The bulk and the flat part of the sample were composed of equiaxed grains. Elongated grains were found in the rolled edge close to the surface. No grain refinement was observed.

2.2 Hardening distribution

2.2.1 Reference shot peened zone

Figures 4 (a) and (b) show the GND distributions estimated in the reference zone at a minimum distance of 150 μm from the rolled edge with conventional Hough and dictionary indexing respectively. Figure 5 shows the relative position of the different maps shown in Figure 4 for better clarity. Both methods exhibited a GND density gradient from the surface to the bulk due to shot peening induced work hardening. The density gradient is however more

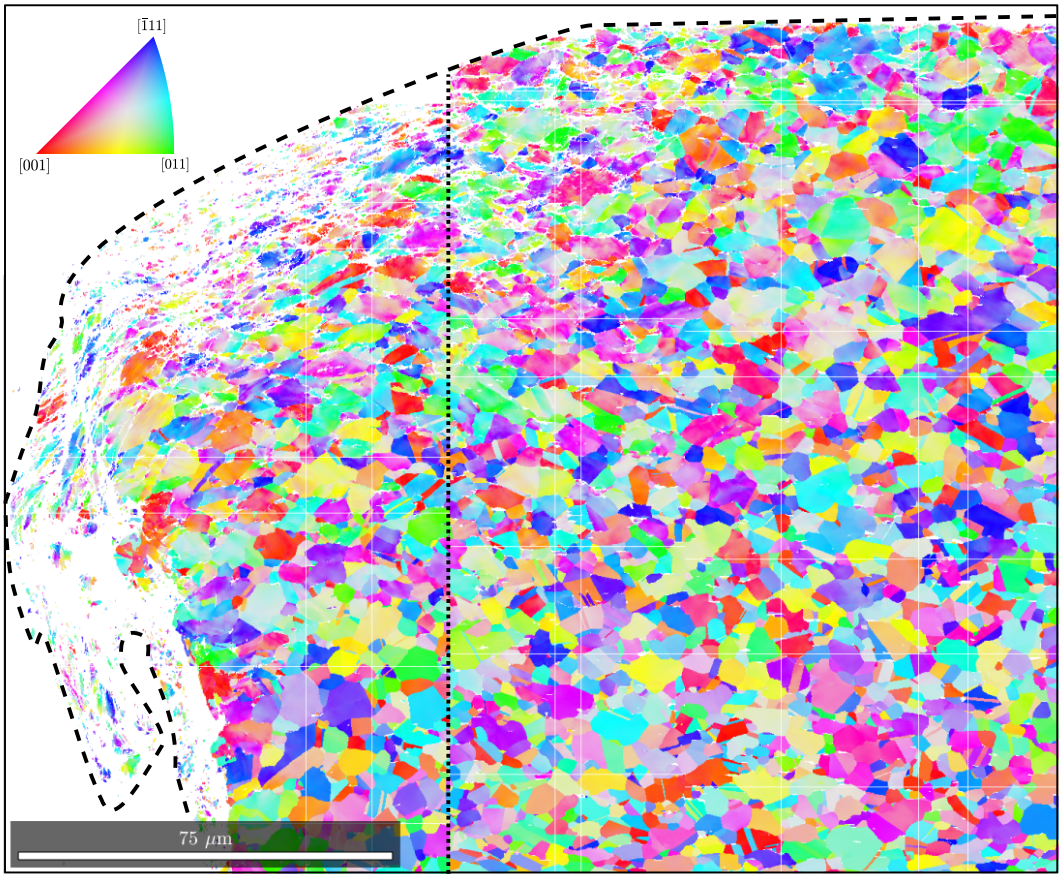

Figure 3: Inverse Pole Figure (IPF) map relative to the sample's normal obtained next to the rolled edge zone. Dashed lines represents the samples border to emphasize the zones that were not indexed. Elongated grains are observed next to the surface at the edges. The dotted line represents the limit between the two EBSD acquisitions. A drift in the orientation data due to the long acquisition time can be observed close to this limit at the bottom of the map.

pronounced when using the dictionary indexing method. Figures 4 (c) and (d) show the GND density distribution estimated in the bulk using Hough and dictionary indexing, respectively. The average density observed in the bulk qualitatively matches those represented at the lower depths in Figure 4 (a) and (b). This reveals that the maps acquired for the shot peened reference captured the whole surface gradient induced by shot peening. This is confirmed by Figure 6 which shows the average GND density depth profiles computed on 15 μm high bands at different depths. The average bulk GND density was 4.2 10^{14} m^{-2} using DI and 7.7 10^{14} m^{-2} using Hough indexing. The affected depth is therefore 125 μm deep.

Figure 6 quantitatively reveals the GND gradient induced by shot peening work hardening from the surface to the bulk. As already visible in Figure 4, the main difference between the two indexing methods was found in the bulk. The average density estimated using Hough

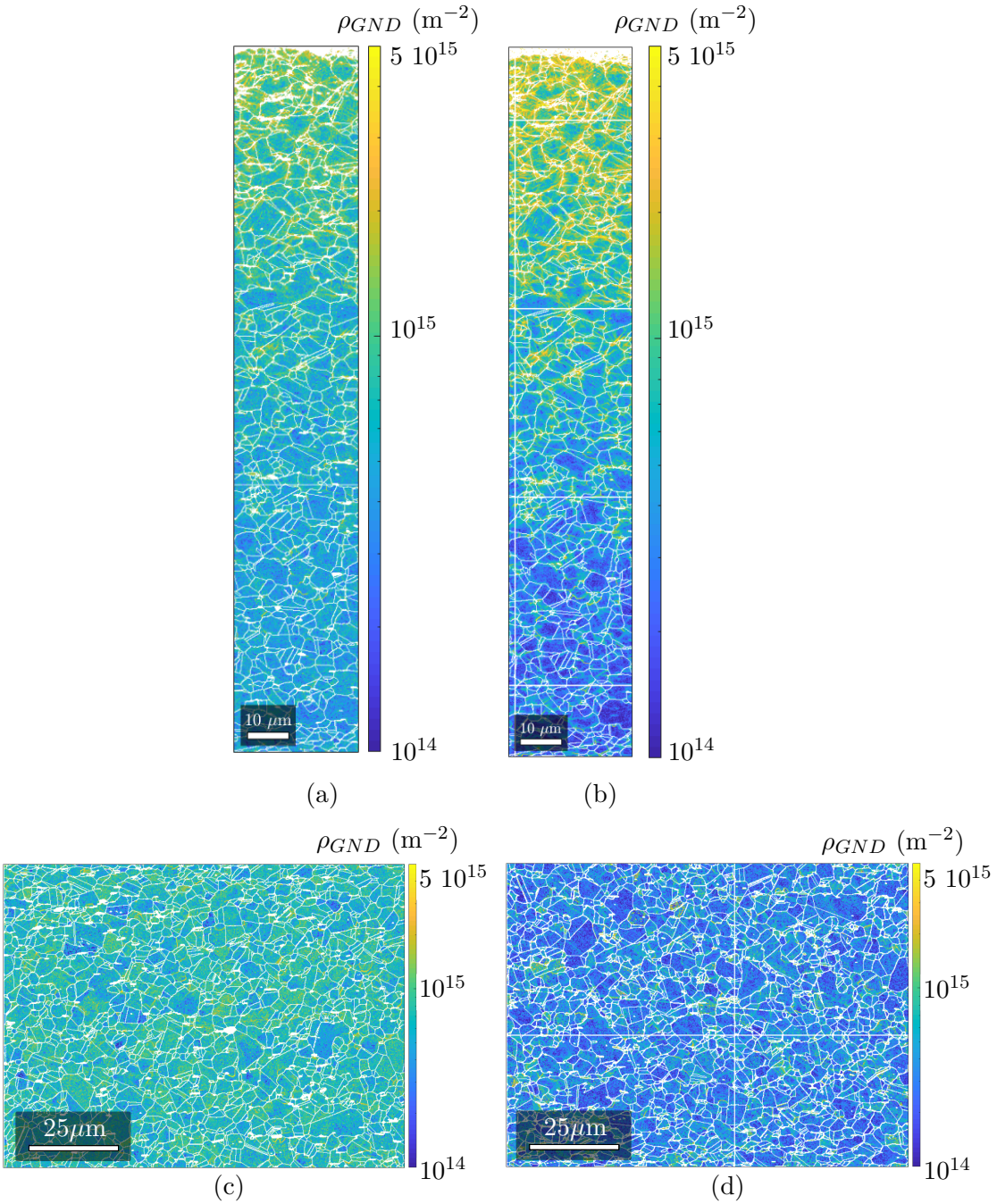

Figure 4: GND density map estimated far from the sample edges close to the surface and in the bulk using (a)(c) conventional Hough transform and (b)(d) Dictionary indexing. Both figures reveals a hardening gradient induced by shot peening from the surface to the bulk. The dictionary indexing approach provides a better contrast inside each grain and reveals a higher dislocation density gradient. The average dislocation density observed at the bottom of (b) seems to match the average hardening level of the sample bulk.

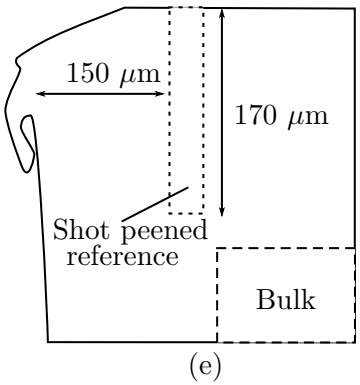

Figure 5: Position of the two different EBSD maps represented in Figure 4. The dotted lines represents the shot peened reference zone close to the surface. The dashed lines represents the bulk zone.

.

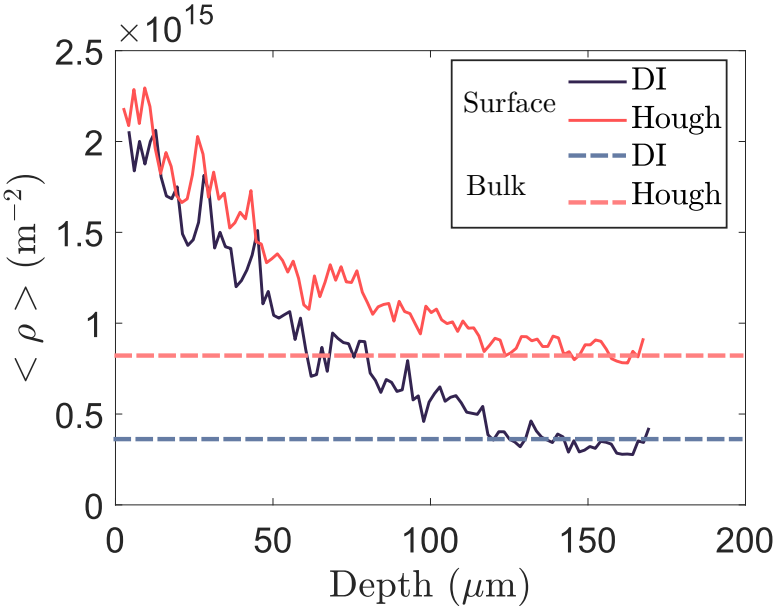

Figure 6: GND density average variations with depths using conventional Hough transform and Dictionary indexing. A higher GND density gradient is quantitatively found using DI. Higher density values in the bulk using conventional Hough transform result from higher noise on the orientation values.

indexing was 1.8 times higher, when compared to that obtained with DI. Such difference could be explained by spurious dislocation density due to noisy orientation data in the bulk when using conventional Hough transform. DI should therefore provide a better estimation of the GND density.

A Taylor hardening model was used to compare the estimated GND density gradient with experimentally measured hardening gradients. GND density ρ_{GND} was related to the critical

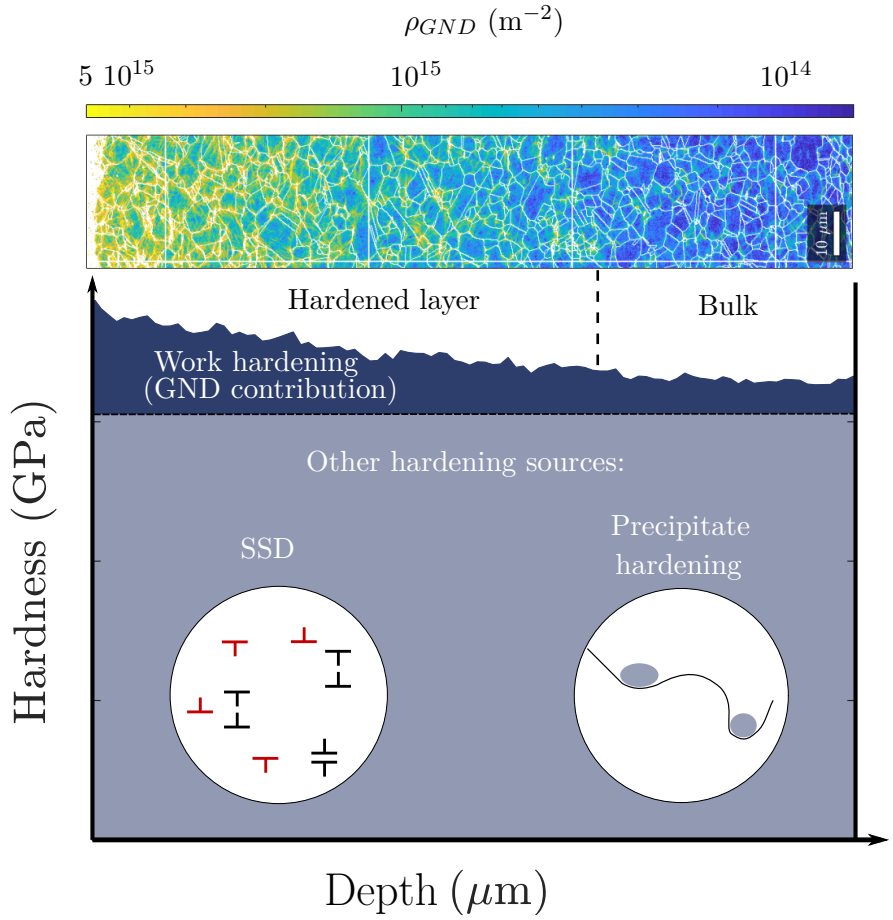

Figure 7: Shot peened IN718 specimen sources of hardening. EBSD estimations only provides insights in the work hardening GND contribution to the global hardness, represented as the dark blue area. This contribution is small compared to other contributions such as precipitate hardening or the presence of SSD, represented by the gray area. Indentation measurements are representative of both areas. The contribution of GND induced work hardening on the hardening gradient can be extracted using EBSD based GND estimations.

resolved shear stress τ_c in a given system with:

$$\tau_c = \alpha G b \sqrt{\rho_{GND}}, \tag{5}$$

where α is an empirical constant representative of the plasticity mechanism, taken as 0.3, as suggested by Mughrabi [28], and G is the material shear modulus taken as 76 GPa. The critical resolved shear stress was then related to the material's hardness H using Tabor's relation as:

$$H = 3\sigma_y, \tag{6}$$

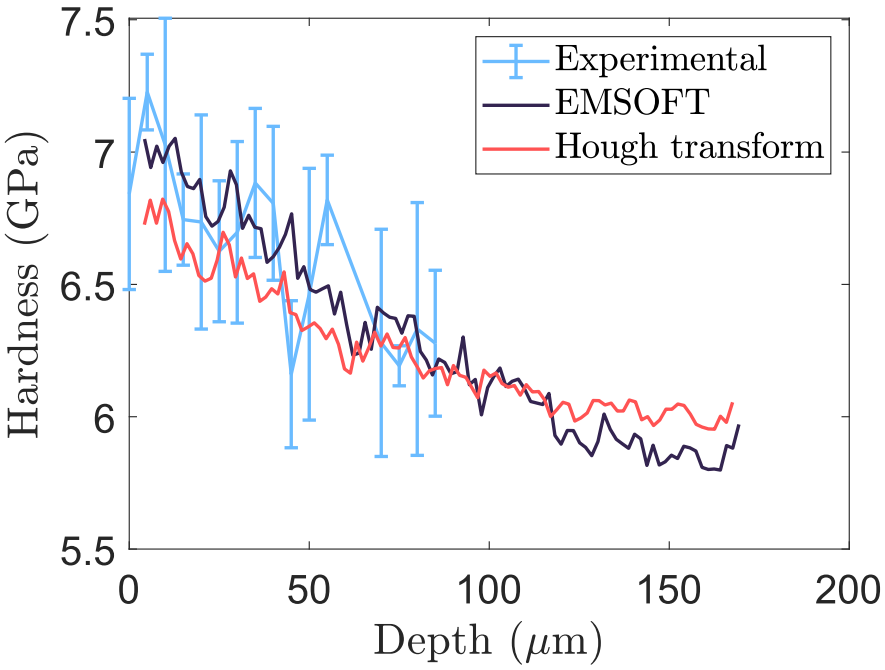

Figure 8: Comparison between experimentally measured indentation hardness and hardness estimations from the EBSD GND densities. The difference between the indentation measured hardness and the GND estimations at 90 μm depth was added to the estimated hardness to compare only the hardness gradient resulting from the dislocation density gradient, without accounting for other sources of hardening. Experimental hardness have a large dispersion. The estimated hardness gradient follows well the experimental one for both indexing methods.

where σ_y is the material's yield stress estimated as:

$$\sigma_y = \frac{1}{m}\tau_c, \tag{7}$$

where m is the Schmid factor, which was here assumed as constant and taken as $\frac{1}{\sqrt{6}}$. Such relations do not provide a quantitative assessment of the hardness absolute value using the GND density as they are purely empirical and rely on strong hypotheses. They however provide an order of magnitude of the hardness gradient resulting from shot peening induced work hardening.

Also, this estimation only accounts for GND induced Taylor work hardening and not for other contributions such as precipitate hardening which is predominant for the studied material. As schematized in Figure 7, these other contributions have to be added to the estimated hardness value to be compared to experimental hardness. To compare only the

hardening gradient, the indentation measured hardness value at 90 μm depth was added to the GND estimated hardness.

Figure 8 shows the comparison of experimentally measured hardness values with the GND estimations using both indexing methods. Fifteen different indentations at constant depth were averaged for each hardness value. Despite the large variability of the indentation hardness measurements, a good correspondence can be found with the GND estimations for both methods. The difference in GND densities observed between Hough indexation and Dictionary indexing only resulted in a 300 MPa hardness difference, which is negligible when compared to the material's hardness.

2.2.2 Rolled edge zone

Figure 9 shows the GND density distribution close to the rolled edge. Higher densities were observed close to the rolled edge as compared to the flat part of the sample. Also, severe

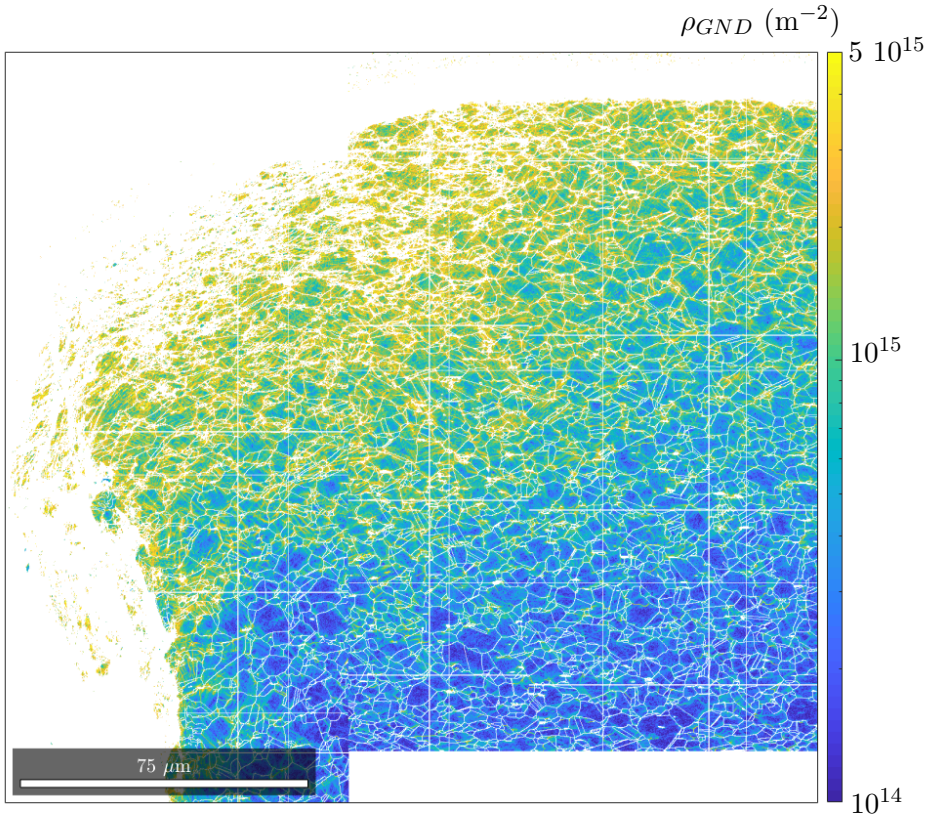

Figure 9: GND distribution in the rolled edge estimated using dictionary indexing. Higher density values can be observed next to the rolled edge than in the shot peened reference.

plastic deformation close to the rolled edge surface prevented the EBSD indexing.

To compare the material hardening state between the reference and the rolled edge at the same depth, a depth map between a given point and the sample surface was computed as shown in Figure 10 (a). The sample's surface was drawn manually using Bezier Curves

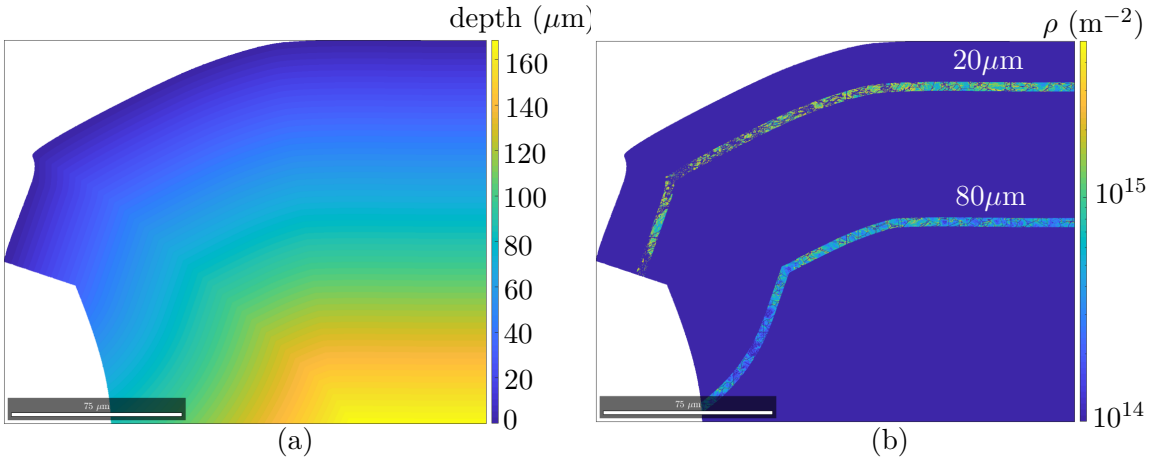

Figure 10: (a)Depth map computed for the rolled edge zone to compare average dislocation values between the rolled edge and the reference at the same depths, despite the geometry of the rolled edge. (b)GND density maps on two bands taken at 20 µm and 80 µm. Average dislocation density variation from the edge to the sample center was computed on the two bands by computing the dislocation average on 100 slices of those bands.

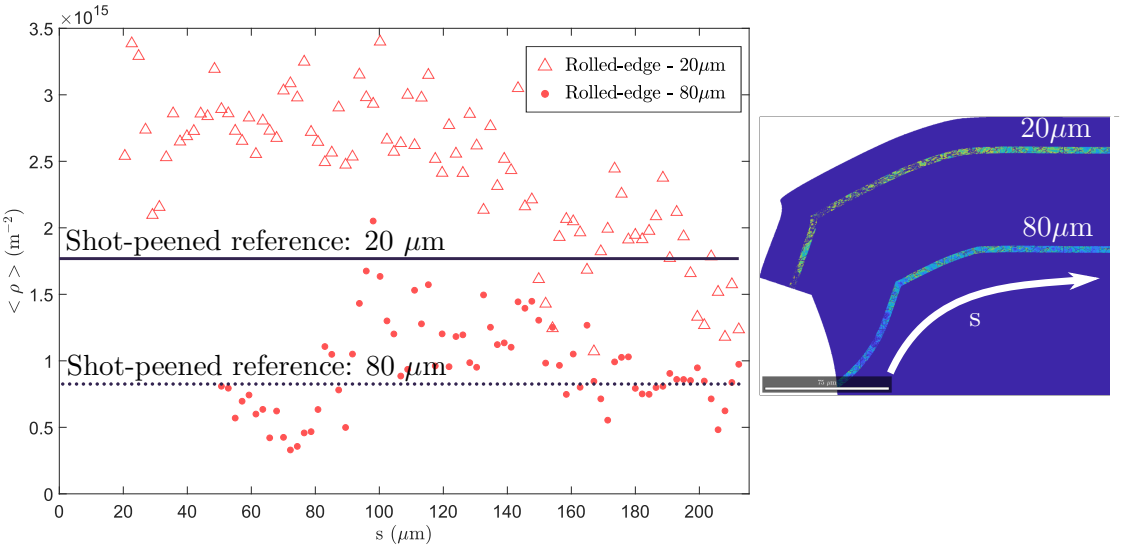

Figure 11: Average GND density variation from the rolled edge (s=0µm) to the reference zone (s=220 µm) with the curvi-linear abscissa s following the bands presented in figure 10. Decrease in the dislocation density from the edge to the center can be observed at 20 µm depths. The dislocation density at 80 µm is almost constant from the rolled edge to the sample's center.

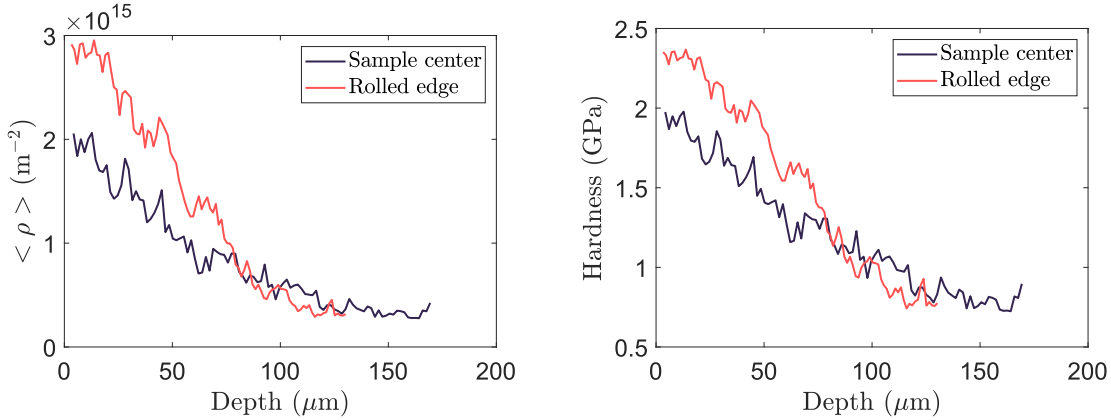

Figure 12: (a) Average GND density variation with the depth represented in Figure 10(a) next to the rolled edge ($0 \leq s \leq 90$ μm) and in the reference zone (190 $\mu m \leq s \leq 220$ μm). (b) Taylor hardening estimations in the rolled edge and reference zones. Higher GND densities are found close to the rolled edge beneath the surface. This results in hardening differences of roughly 400 MPa at the surface between the rolled edge and the reference zone.

with the Inkscape [1] software . The minimal distance between a given point and the curve was then computed using a Matlab script. This provided GND density data bands at a given depth such as those shown in Figure 10 (b).

Figure 11 shows the average GND density variation from the rolled edge to the sample center at 20 μm and 80 μm depths. The figure confirms that higher dislocation density values are found close to the rolled edge. Figure 12 (a) shows a comparison between the GND density variation with depth, close to the rolled edge and in the reference zone. The resulting Taylor hardening estimation is shown in Figure 12 (b). This further confirms the results shown in Figure 11. It also reveals that the density gradient is higher in this zone, as the same bulk density was found at similar depths as in the reference zone. Figure 12 reveals that such GND gradients could result in hardness differences of 500 MPa close to the surface.

Figure 13 (a) shows a comparison between experimentally measured hardness in the rolled edge at three different locations and in the reference at two different locations, as detailed in Figure 13 (b). Five hardness measurements at a given depth were averaged for each hardness value. The figure reveals an average subsurface hardness increase of 1 GPa between the rolled edge and the reference. This confirms the results obtained using GND estimations from EBSD analyses. Let us note that the order of magnitude is correct even though there is a 500 MPa difference between both methods. Such a difference could be explained by the low

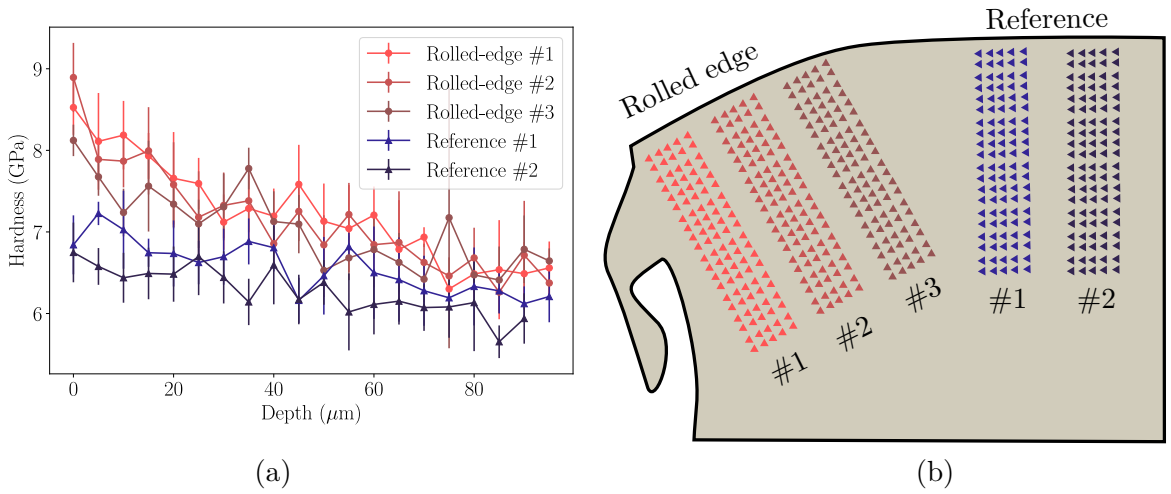

Figure 13: (a) Hardness gradient in the rolled edge and in the reference zone for respectively two and three different indentation tests at different locations sketched in Figure (b). Subsurface hardness increase of 1 GPa in the rolled edge compared with the reference was experimentally observed.

indexation rate obtained next to the rolled edge surface. The choice of a constant Schmid factor, the use of the Taylor hardening law as well as the high indentation measurements standard deviation (326 MPa in average) could also explain such a bias.

Also, it should be noted that EBSD observations do not provide access to the statistically stored dislocation densities, which could also contribute to the observed hardness.

3 Discussion

DI resulted in lower estimated GND densities than those predicted by Hough indexing in the bulk. Such a difference could be attributed to a better performance of the DI method toward noisy patterns. Figure 6 however reveals that similar densities were found by the two methods in the shot peened surface, where the largest plastic deformations should occur. Thus, DI did not improve indexation toward plastic deformation in this case. Also, the difference between the two methods resulted in hardness differences close to the nanoindentation measurement uncertainties. Such differences are therefore negligible when considering hardness estimations. This partly results from the Inconel 718 high hardness resulting from precipitate hardening. Such difference should however be more significant on softer materials and would better assess the relevance of the method.

Also, no filter was used on the orientation data to improve the GND density estimation in this study. Local filters such as the local linear adaptation of smoothing splines developed by Seret et al. [35] could help reducing the influence of noise on GND estimations while preserving the GND structures.

A difference of 500 MPa was found between the hardness variations estimated from GND densities and that measured by nanoindentation in the rolled edge. These differences could be explained by the fact that the Taylor model used in this study relies on the assumption that a constant Schmid factor characterizes the whole probed surface. Despite the good correspondence of the hardness gradients observed far from the rolled edge in Figure 8, these differences could also be explained by the potential contribution of the SSD densities to work hardening, which cannot be estimated using EBSD measurements. However, both hardness gradients estimated from GND and obtained by nanoindentation were more pronounced in the vicinity of the bulge zone. This confirms that part of the observed differences in hardness between the bulge and the flat zone can be explained by the GND contribution to work hardening.

The observed hardness difference between GND estimations and nano-indentation measurement could also result from an evolution of the Inconel 718 Direct aged γ'' precipitates morphology and interface properties during the process induced by severe plastic deformations [27, 33, 46]. In this work, it was assumed that the strains imposed by the shot peening treatment performed were sufficiently small to prevent such effect, as the plastic strain amplitude should not exceed 45% with the peening conditions used, as shown by Goulmy et al. [14]. The potential influence of this effect on the observed hardness gradient in the rolled edge zone will be further investigated in future works.

Microstructural evolution induced by severe plastic deformation is related to the shearing mechanisms imposed to the material. According to Segal et al. [34], simple shear leads to grain rigid body rotations and favors grain refinement. Inversely, pure shear results in higher grain size ratio and higher intragranular dislocation densities. Figure 14 (a) and (b) respectively show the variation of the grain area and the Grain Average Misorientation (GAM) as a function of depth in the viscinity of the rolled edge, for depths deeper than 25 μm. Observation of Figure 14 confirms that grains close to the rolled edge exhibited

higher dislocation densities and an absence of grain refinement. Such microstructure therefore resulted from a pure shear state induced by shot peening close to the specimen's border.

Figure 15 summarizes the proposed deformation mechanism leading to the rolled edge microstructural state. As opposed to the reference zone, represented in dark blue in Figure 16, the impacts occurred on a partially free surface. Therefore, early shot induce material stretching, which produces a bulge where the material is free to deform. When the initiated bulge is further impacted, a global bending develops in the bulge zone, which leads to a rolled edge and to a highly sheared zone as depicted in Figure 16. Since the highly sheared zone

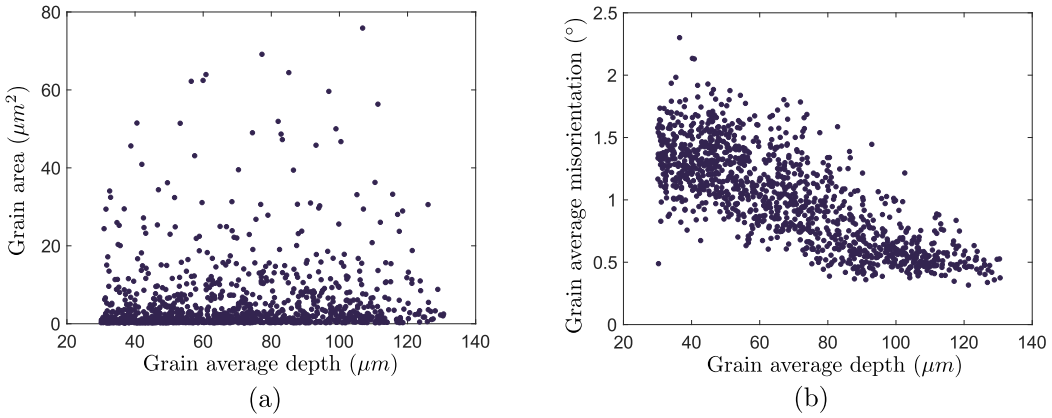

Figure 14: (a) Grain area variation and (b) Grain Average Misorientation (GAM) variationsas a function of depth, in the viscinity of the rolled edge. The grain area is relatively constant while the GAM continuously decreases as the depth increases.

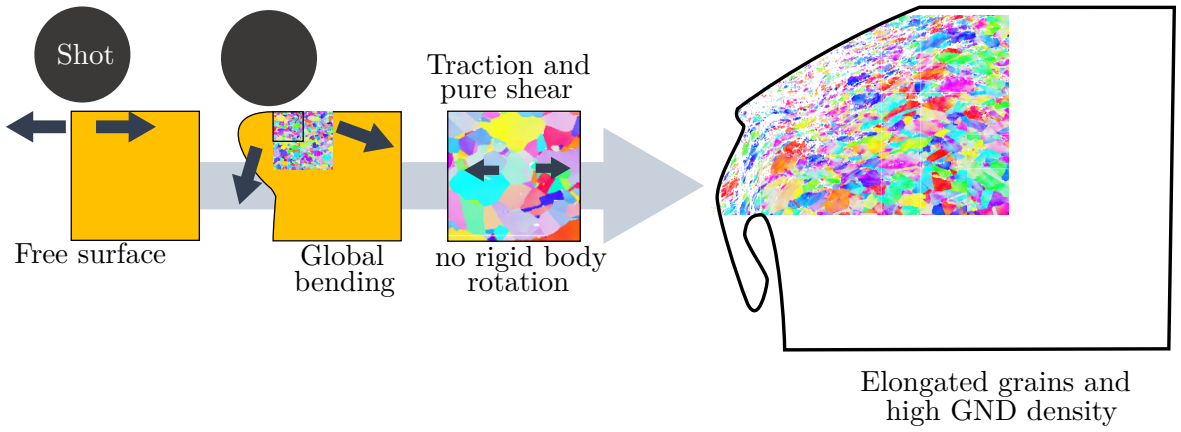

Figure 15: Summary of the proposed deformation mechanism in the rolled edge. Early shots induces surface stretching bulging the surface where the material is free to deform. When further impacted, stretching results in a global bending of the forming rolled edge. This induces pure shear stress state in the grains.

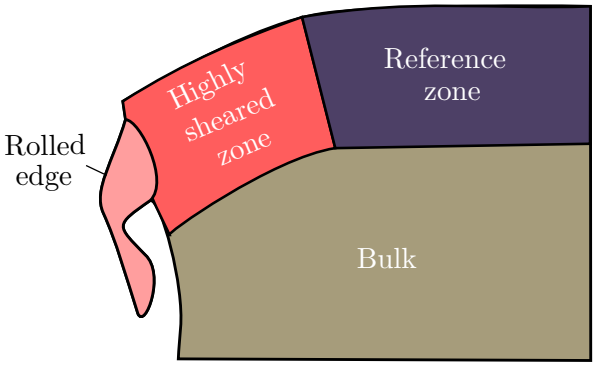

Figure 16: Summary of the different hardening areas induced by shot peening of an edge. Higher GND densities and hardening gradient than that found in the reference zone was induced by the pure shear state close to the edge. The induced rolled edge being more free the deform suffer was subjected to less shear when further impacted as compared to the highly sheared zone.

is free to rotate, individual grains experience no rigid body rotation. Such bending induces high tensile stresses in the rolled edge grains, resulting in a pure shear stress state, as the deforming grains are blocked by the bulk. This results in highly elongated grains and a high dislocation density in the highly sheared zone. Such mechanism is similar to that observed by Mattei et al. [26] after microstructural analysis of a highly bent AA6016 sheet. Once formed, the rolled edge is more free to deform as opposed to the highly sheared zone and is therefore less subjected to shear when further impacted.

These differences in hardening could have an influence on the treated parts' fatigue life. Klotz et al. [21] investigated the influence of shot peening induced hardening and residual stresses on the Inconel 718 alloy fatigue life. The authors found that shot peening induced cold work reduces the negative effect resulting from surface roughness in the LCF regime. The hardening state of the Inconel 718 sample has therefore a critical impact on its LCF life properties, independently of the residual stresses induced in the material. In the present study, work hardening has a negligible influence on the Inconel 718 properties compared to precipitate hardening. The increased hardness observed in the present work should therefore only have little effect on the material's fatigue life in the LCF regime.

Also, for the Inconel 718, the influence of the rolled edge higher hardening values on the fatigue life should be negligible in the HCF regime, as it is mainly driven by the materials' residual stress state, as evidenced by Klotz et al. [21]. Eleiche et al. [10] performed High Cycle Fatigue (HCF) tests on flat shot peened high strength martensitic steel specimens for

which the residual stresses had been relaxed by a thermal treatment. Shot peened specimens presented a 20% fatigue life improvement, when compared to as-received specimens. However, the residual stress relaxation only degraded the material's fatigue life by 3%. The increased hardness observed in the rolled edge could therefore have an impact on the HCF fatigue life of such materials.

Higher dislocation densities could also have an effect on the corrosion properties of the treated material. Naeini et al. [29] studied the pitting resistance of an accumulative roll bonded 5052 aluminum alloy sample. An increase in dislocation density resulted in a less protective oxide layer hence degrading the material's resistance to corrosion. Similar results were also found by Singh et al. [36] after cold rolling of an AISI304 steel and also by Laleh et al. [23] on a AZ91D magnesium alloy after Surface Mechanical Attrition Treatment (SMAT). The higher hardening state of the rolled edge as well as its non-linear shape could therefore have a negative impact on the treated part's corrosion resistance.

Finally, as evidenced by Figure 11, the rolled-edge formation influences the sample's hardening gradient in a zone surrounding the edge, and not solely inside the rolled-edge. This reveals that removing the rolled edge, as suggested by You et al. [45], would not entirely remove the hardening heterogenities resulting from its formation.

4 Conclusion

The objective of this work was to study the mechanical behaviour of a shot peened induced rolled edge as compared to a flat shot peened zone for the Inconel 718 alloy. The main contribution are:

- DI indexed EBSD maps presented lower GND densities than those obtained from Hough indexing. This was attributed to spurious GND densities due to noisier orientation data when using Hough indexing.
- Nanoindentation hardness measurements revealed that shot peening induced rolled edges present a hardness increase of 1 GPa and a higher hardness gradient as compared to the reference zone.

- This hardening was directly related to the GND densities estimated in the rolled edge using a Taylor hardening model. This revealed that the measured hardness increase is mainly due to work hardening.
- The rolled edge surface presented elongated grains which might be explained by a pure shear state imposed to the material during severe plastic deformation.
- Such hardening and microstructural heterogeneities were not only found in the rolled-edge but also in its surrounding.
- Comparison between GND gradient maps and nanoindentation data provided a methodology to assess the process influence on complex geometries which is crucial to understand potential effects on the treated parts fatigue's life or corrosion resistance.

The zone surrounding a shot peened induced rolled edge could therefore present different fatigue and corrosion resistance properties than a flat shot peened zone, even after the removal of the excess of matter. This influence should however be investigated through HCF and LCF fatigue tests on material for which work hardening is predominant, such as martensitic stainless steel or alpha-iron alloys, as well as corrosion tests, to confirm this influence.

Data availability

The raw/processed data required to reproduce these findings cannot be shared at this time due to legal or ethical reasons.

Acknowledgement

This work was supported by the Natural Sciences and Engineering Research Council (NSERC) discovery grants Canada Research Chairs programs (grant number, RGPIN-06412-2016); and the Region Auvergne-Rhône-Alpes within the SCUSI project.

References

[1] Harrington, B. et al. (2004-2005). Inkscape. http://www.inkscape.org/, 2004.

[2] A. Acharya and R. J. Knops. An observation on the experimental measurement of dislocation density. *Journal of Elasticity*, 114(2):275–279, Feb 2014.

[3] Y. Al-Obaid. The effect of shot peening on stress corrosion cracking behaviour of 2205-duplex stainless steel. *Engineering Fracture Mechanics*, 51(1):19 – 25, 1995.

[4] F. Bachmann, R. Hielscher, and H. Schaeben. Texture analysis with mtex – free and open source software toolbox. In *Texture and Anisotropy of Polycrystals III*, volume 160 of *Solid State Phenomena*, pages 63–68. Trans Tech Publications Ltd, 3 2010.

[5] M. Burch, C. Fancher, S. Patala, M. De Graef, and E. Dickey. Mapping 180° polar domains using electron backscatter diffraction and dynamical scattering simulations. *Ultramicroscopy*, 173:47–51, 2017.

[6] S. Coratella, M. Sticchi, M. Toparli, M. Fitzpatrick, and N. Kashaev. Aplication of the eigenstrain approach to predict the residual stress distribution in laser shock peened aa7050-t7451 samples. *Surface & Coatings Technology*, 273:39–49, 2015.

[7] S. Das, F. Hofmann, and E. Tarleton. Consistent determination of geometrically necessary dislocation density from simulations and experiments. *International Journal of Plasticity*, 109:18 – 42, 2018.

[8] M. De Graef, W. Lenthe, N. Schäfer, T. Rissom, and D. Abou-Ras. Unambiguous determination of local orientations of polycrystalline $cuinse_2$ thin films via dictionary-based indexing. *Physica status solidi (RRL)–Rapid Research Letters*, page 1900032, 2018.

[9] A. Dewald and M. Hill. Eigenstrain-based model for prediction of laser peening residual stresses in arbitrary three-dimensional bodies. part 1: model description. *Journal of Strain Analysis*, 44, 2009.

[10] A. M. Eleiche, M. M. Megahed, and N. M. Abd-allah. The shot-peening effect on the HCF behavior of high-strength martensitic steels. *Journal of Materials Processing Technology*, 113(1-3):502–508, 2001. 5^{th} Asia-Pacific Conference on Materials Processing, Seoul, South Korea, 2001.

[11] D. Gallitelli, V. Boyer, M. Gelineau, Y. Colaitis, E. Rouhaud, D. Retraint, R. Kubler, M. Desvignes, and L. Barrallier. Simulation of shot peening: from process parameters to residual stress fields in a structure. *Comptes Rendus Mécanique*, 344(4):355 – 374, 2016. Computational simulation of manufacturing processes.

[12] M. Gelineau, L. Barrallier, E. Rouhaud, R. Kubler, and Q. Puydt. Residual stress field prediction in shot peened mechanical parts with complex geometries. In T. Holden, O. Muransky, and L. Edwards, editors, *Residual Stresses 2016: ICRS-10*, volume 2 of *Materials Research Proceedings*, pages 49–54, 2017.

[13] A. Ghasemi, S. M. Hassani-Gangaraj, A. H. Mahmoudi, G. H. Farrahi, and M. Guagliano. Shot peening coverage effect on residual stress profile by FE random impact analysis. *Surface Engineering*, 32(11):861–870, 2016.

[14] J. Goulmy, P. Kanoute, E. Rouhaud, L. Toualbi, S. Kruch, V. Boyer, J. Badreddine, and D. Retraint. A calibration procedure for the assessment of work hardening part ii: Application to shot peened in718 parts. *Materials Characterization*, 175:111068, 2021.

[15] G. Guillonneau, G. Kermouche, S. Bec, and J.-L. Loubet. Extraction of mechanical properties with second harmonic detection for dynamic nanoindentation testing. *Experimental Mechanics*, 52(7):933–944, 2012.

[16] R. Haynes. The influence of residual stress due to shot peening on the fatigue behaviour of silicon manganese spring steel. *Strain*, 3(4):3–11, 1967.

[17] B. He, K. Soady, B. Mellor, A. Morris, and P. Reed. Effects of shot peening on short crack growth rate and resulting low cycle fatigue behaviour in low pressure turbine blade material. *Materials Science and Technology*, 29(7):788–796, 2013.

[18] J. Hu, Z. Liu, E. V. der Giessen, and Z. Zhuang. Strain rate effects on the plastic flow in submicron copper pillars: Considering the influence of sample size and dislocation nucleation. *Extreme Mechanics Letters*, 17:33 – 37, 2017.

[19] M. A. Jackson, E. Pascal, and M. De Graef. Dictionary indexing of electron back-scatter diffraction patterns: a hands-on tutorial. *Integrating Materials and Manufacturing Innovation*, 8(2):226–246, Jun 2019.

[20] Z. Jiabin, L. Shihong, W. Tianrui, Z. Zhen, and Z. Wei. An evaluation on SP surface property by means of combined FEM-DEM shot dynamics simulation. *Advances in Engineering Software*, 115:283–296, JAN 2018.

[21] T. Klotz, D. Delbergue, P. Bocher, M. Lévesque, and M. Brochu. Surface characteristics and fatigue behavior of shot peened inconel 718. *International Journal of Fatigue*, 110:10 – 21, 2018.

[22] T. Klotz, M. Lévesque, and M. Brochu. Effects of rolled edges on the fatigue life of shot peened inconel 718. *Journal of Materials Processing Technology*, 2018.

[23] M. Laleh and F. Kargar. Effect of surface nanocrystallization on the microstructural and corrosion characteristics of az91d magnesium alloy. *Journal of Alloys and Compounds*, 509(37):9150 – 9156, 2011.

[24] H. Lieurade and A. Bignonnet. Fundamental aspects of the effect of shot peening on the fatigue strength of metallic parts and structures. In *3rd International Conference on Shot Peening, Garmisch-Partenkirchen, Germany*, pages 343–360, 1987.

[25] V. Llaneza and F. Belzunce. Study of the effects produced by shot peening on the surface of quenched and tempered steels: roughness, residual stresses and work hardening. *Applied Surface Science*, 356:475 – 485, 2015.

[26] L. Mattei, D. Daniel, G. Guiglionda, H. Klöcker, and J. Driver. Strain localization and damage mechanisms during bending of aa6016 sheet. *Materials Science and Engineering: A*, 559:812 – 821, 2013.

[27] Y. Mei, Y. Liu, C. Liu, C. Li, L. Yu, Q. Guo, and H. Li. Effects of cold rolling on the precipitation kinetics and the morphology evolution of intermediate phases in inconel 718 alloy. *Journal of Alloys and Compounds*, 649:949–960, 2015.

[28] H. Mughrabi. The alpha-factor in the taylor flow-stress law in monotonic, cyclic and quasi-stationary deformations: Dependence on slip mode, dislocation arrangement and density. *Current Opinion in Solid State and Materials Science*, 20(6):411 – 420, 2016. the COSSMS Twentieth Anniversary Issue.

[29] M. F. Naeini, M. H. Shariat, and M. Eizadjou. On the chloride-induced pitting of ultra fine grains 5052 aluminum alloy produced by accumulative roll bonding process. *Journal of Alloys and Compounds*, 509(14):4696 – 4700, 2011.

[30] W. Oliver and G. Pharr. An improved technique for determining hardness and elastic modulus using load and displacement sensing indentation experiments. *Journal of Materials Research*, 7(6):1564–1583, 1992.

[31] V. Pandey, J. Singh, K. Chattopadhyay, N. S. Srinivas, and V. Singh. Influence of ultrasonic shot peening on corrosion behavior of 7075 aluminum alloy. *Journal of Alloys and Compounds*, 723:826 – 840, 2017.

[32] W. Pantleon. Resolving the geometrically necessary dislocation content by conventional electron backscattering diffraction. *Scripta Materialia*, 2008.

[33] M. A. Ramalho Medeiros, C. H. de Melo, A. L. Pinto, L. H. de Almeida, and L. S. Araújo. The delta phase precipitation during processing and the influence on grain boundary character distribution and mechanical properties of superalloy 718. *Materials Science and Engineering: A*, 726:187–193, 2018.

[34] V. M. Segal. Equivalent and effective strains during severe plastic deformation (spd). *Philosophical Magazine Letters*, 98(11):511–520, 2018.

[35] A. Seret, C. Moussa, M. Bernacki, J. Signorelli, and N. Bozzolo. Estimation of geometrically necessary dislocation density from filtered EBSD data by a local linear adaptation of smoothing splines. *Journal of Applied Crystallography*, 52(3):548–563, Jun 2019.

[36] R. Singh. Influence of cold rolling on sensitization and intergranular stress corrosion cracking of aisi 304 aged at 500 degree c. *Journal of Materials Processing Technology*, 206(1):286 – 293, 2008.

[37] S. Singh, Y. Guo, B. Winiarski, T. Burnett, P. Withers, and M. DeGraef. High resolution low kv ebsd of heavily deformed and nanocrystalline aluminium by dictionary-based indexing. *Scientific Reports*, 2018.

[38] R. Sun, Z. Che, Z. Cao, S. Zou, J. Wu, W. Guo, and Y. Zhu. Fatigue behavior of Ti-17 titanium alloy subjected to different laser shock peened regions and its microstructural response. *Surface and Coatings Technology*, 383:125284, 2020.

[39] F. Tu, D. Delbergue, H. Miao, T. Klotz, M. Brochu, P. Bocher, and M. Levesque. A sequential dem-fem coupling method for shot peening simulation. *Surface and Coatings Technology*, 319(Supplement C):200 – 212, 2017.

[40] D. Tumbajoy-Spinel, S. Descartes, J.-M. Bergheau, H. Al-Baida, C. Langlade, and G. Kermouche. Investigation of graded strengthened hyper-deformed surfaces by impact treatment: micro-percussion testing. *IOP Conference Series: Materials Science and Engineering*, 194(1):012024, 2017.

[41] D. Tumbajoy-Spinel, X. Maeder, G. Guillonneau, S. Sao-Joao, S. Descartes, J.-M. Bergheau, C. Langlade, J. Michler, and G. Kermouche. Microstructural and micromechanical investigations of surface strengthening mechanisms induced by repeated impacts on pure iron. *Materials & Design*, 147:56 – 64, 2018.

[42] A. J. Wilkinson and D. Randman. Determination of elastic strain fields and geometrically necessary dislocation distributions near nanoindents using electron back scatter diffraction. *Philosophical Magazine*, 90(9):1159–1177, 2010.

[43] S. Wright, M. Nowell, S. Lindeman, P. Camus, M. De Graef, and M. Jackson. Introduction and comparison of new ebsd post-processing methodologies. *Ultramicroscopy*, 159:81–94, 2015.

[44] Y. Wu, B. Guelorget, Z. Sun, R. Déturche, and D. Retraint. Characterization of gradient properties generated by smat for a biomedical grade 316l stainless steel. *Materials Characterization*, 155:109788, 2019.

[45] C. You, M. Achintha, K. Soady, and P. Reed. Low cycle fatigue life prediction in shot-peened components of different geometries – part ii: life prediction. *Fatigue and Fracture and Engineering Materials and Structures*, 40:749–760, 2016.

[46] H. Zhang, C. Li, Q. Guo, Z. Ma, H. Li, and Y. Liu. Improving creep resistance of nickel-based superalloy inconel 718 by tailoring gamma double prime variants. *Scripta Materialia*, 164:66–70, 2019.

[47] X. Zhang, N. Hansen, Y. Gao, and X. Huang. Hall–petch and dislocation strengthening in graded nanostructured steel. *Acta Materialia*, 60(16):5933 – 5943, 2012.